



Towards electrochemical hydrogen storage in liquid organic hydrogen carriers via proton-coupled electron transfers

Hamid Ghorbani Shiraz^{a,1}, Mikhail Vagin^{a,*,1}, Tero-Petri Ruoko^{a,b}, Viktor Gueskine^a, Krzysztof Karoń^c, Mieczysław Łapkowski^c, Tobias Abrahamsson^a, Thomas Ederth^d, Magnus Berggren^a, Xavier Crispin^{a,*}

^a Laboratory of Organic Electronics, Department of Science and Technology (ITN), Linköping University, SE-601 74 Norrköping, Sweden

^b Smart Photonic Materials, Faculty of Engineering and Natural Sciences, Tampere University, P. O. Box 541, Tampere FI-33101, Finland

^c Silesian University of Technology, Faculty of Chemistry, Department of Physical Chemistry and Technology of Polymers, M. Strzody 9, 44-100 Gliwice, Poland

^d Department of Physics, Chemistry and Biology (IFM), Linköping University, SE-581 83 Linköping, Sweden

ARTICLE INFO

Article history:

Received 26 April 2022

Revised 8 June 2022

Accepted 10 June 2022

Available online 18 June 2022

Keywords:

Proton-coupled electron transfer
Electrochemical hydrogen storage
Hydrogen bonding agent
Anion-radical
Comproportionation

ABSTRACT

Green hydrogen is identified as one of the prime clean energy carriers due to its high energy density and a zero emission of CO₂. A possible solution for the transport of H₂ in a safe and low-cost way is in the form of liquid organic hydrogen carriers (LOHCs). As an alternative to loading LOHC with H₂ via a two-step procedure involving preliminary electrolytic production of H₂ and subsequent chemical hydrogenation of the LOHC, we explore here the possibility of electrochemical hydrogen storage (EHS) via conversion of proton of a proton donor into a hydrogen atom involved in covalent bonds with the LOHC (R) via a proton-coupled electron transfer (PCET) reaction: $2nH^+ + 2ne^- + R_{ox} \leftrightarrow nH_2R_{red}$. We chose 9-fluorenone/fluorenol (Fnone/Fnol) conversion as such a model PCET reaction. The electrochemical activation of Fnone via two sequential electron transfers was monitored with *in-situ* and operando spectroscopies in absence and in presence of different alcohols as proton donors of different reactivity, which enabled us to both quantify and get the mechanistic insight on PCET. The possibility of hydrogen extraction from the loaded carrier molecule was illustrated by chemical activation.

© 2022 Science Press and Dalian Institute of Chemical Physics, Chinese Academy of Sciences. Published by ELSEVIER B.V. and Science Press. This is an open access article under the CC BY license (<http://creativecommons.org/licenses/by/4.0/>).

1. Introduction

Ecofriendly and safe techniques that convert and store various forms of energy at large scales are prerequisites for a future sustainable society. Hydrogen H₂ is identified as one of the prime clean energy carriers as it expresses high energy density ($E_{H_2} = 33.3 \text{ kWh kg}^{-1}$), when bench-marked versus fossil fuels ($E_{\text{petrol}} = 12 \text{ kWh kg}^{-1}$) [1], and a CO₂ zero-emission as the product of its oxidation is water. Unfortunately, today it is still produced mostly by methane reformation. Furthermore, several drawbacks are hurdles towards the wide spread of hydrogen technology in our society, namely, the high cost of storage and distribution of H₂ because of its low ambient density ($0.089 \text{ kg m}^{-3}@P = 1 \text{ bar}$) and its explosivity (ignition energy = 0.2 mJ) when used in the form of a pressurized gas ($24 \text{ kg m}^{-3}@P = 350 \text{ bar}$) or a cryogenic liquid ($71 \text{ kg m}^{-3}@T = -253 \text{ °C}$).

Hence, to increase the density and avoid explosivity, alternative strategies have been proposed to store H₂ chemically in stable compounds. Water is a perfect non-toxic hydrogen carrier of ultimate density. However, controlled hydrogen release is associated with complex multistep oxygen-associated reactions requiring catalysts. Solid metal hydrides [2] or complex hydrides [3] lead to a storage density of $100\text{--}150 \text{ kg(H}_2\text{) m}^{-3}$ at room temperature and 1 bar through formation of metal-hydrogen bonds. Another interesting class of materials used for hydrogen storage is aromatic organic molecules, also so-called Liquid Organic Hydrogen Carriers (LOHC). The storage takes place through an exothermic hydrogenation reaction at high temperature ($\sim 150 \text{ °C}$) and pressure ($\sim 50 \text{ bar}$) during which the π -bonds are cleaved, and carbon-hydrogen bonds are formed (Fig. 1a). The H₂ gas is released through an endothermic catalytic dehydrogenation at atmospheric pressure (1 bar) and temperature in the range of $50\text{--}300 \text{ °C}$ (Fig. 1a and b) depending on the catalyst and the LOHC. Storage properties are modest with $50\text{--}60 \text{ kg(H}_2\text{) m}^{-3}$ and $5\text{--}7 \text{ wt\% H}_2$ [4] but the molecules are stable and can be transported as liquid fuels in a safe manner. Hence, the transport and storage of H₂ in complex hydrides and organics imply first the production of H₂ by electrolysis, then a hydrogenation step that requires high temperature and pressure (Fig. 1a).

* Corresponding authors.

E-mail addresses: mikhail.vagin@liu.se (M. Vagin), xavier.crispin@liu.se (X. Crispin).

¹ These authors contributed equally to this work.

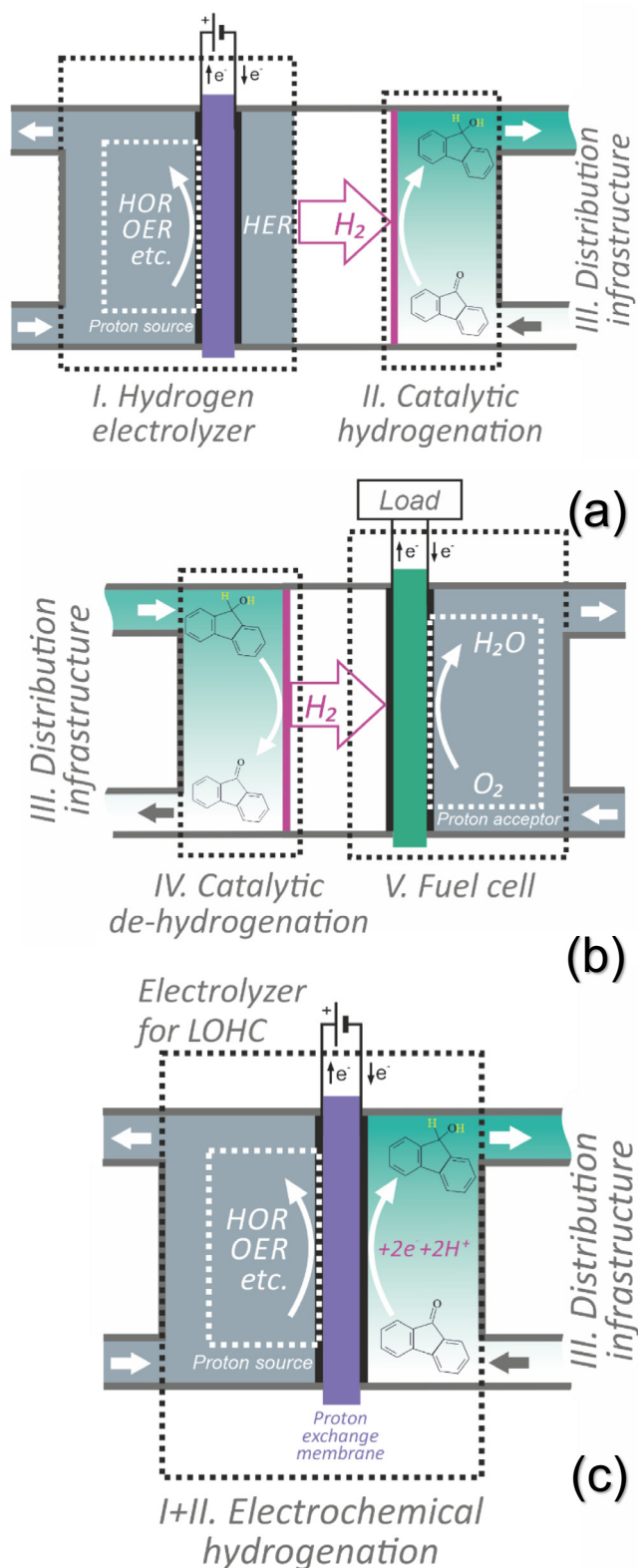


Fig. 1. The H₂ technology simplification by the introduction of the EHS concept in LOHC. (a and b) the main components for H₂ technology: (I) electrolytic hydrogen production, (II) insertion by chemical hydrogenation in LOHC, (III) transportation of LOHC, (IV) chemical hydrogen extraction dehydrogenation and (V) use a fuel cell; (c) simplification by EHS ((I) + (II)).

An interesting strategy to store hydrogen in metals without exposing to H₂ gas is by electrochemical reactions. This is an advantageous method for several reasons: it takes place at room

temperature and atmospheric pressure, and the source of hydrogen is the proton of water upon intercalation and reduction to form metal hydride: $M + xH_2O + xe^- \leftrightarrow MH_x + xOH^-$. The rate of adsorption and release is related to the diffusion coefficient of atomic hydrogen in the metal ($D_H = \sim 10^{-10} \text{ cm}^2 \text{ s}^{-1}$) [5]. Such a reaction has been investigated in depth in the field of Ni-MH batteries [6]. A similar strategy for organic solids has been demonstrated recently. An insoluble organic polymer of fluorenone was reduced electrochemically in acetonitrile electrolyte with a drop of water as source of protons. The release of H₂ from the fluorenone took place with an iridium catalyst in a water/alcohol solution [7].

Here, we propose to replace the traditional hydrogenation of LOHC (Fig. 1a) by an electrochemical hydrogenation of the LOHC (Fig. 1c) through a proton-coupled electron transfer PCET [8], i.e., a reduction of the organic molecule in presence of protons to create a covalent nonmetal-hydrogen bond at room temperature and atmospheric pressure. The electrochemical hydrogen storage (EHS) via PCET on a carrier molecule *R* of even numbers of protons and electrons yields the total reaction:



where *n* is a natural number and *R*_{ox} and *R*_{red} are the oxidized and reduced forms of an organic carrier molecule, respectively.

We chose fluorenone (*Fnone*) as a model high-stability carrier molecule for EHS and studied its PCETs in an aprotic solvent to achieve EHS yielding loaded carrier fluorenone (*Fmol*). The electrochemical activation of *Fnone* via two sequential electron transfers was monitored with *in-situ* spectroscopies in absence and in the presence of different alcohols as proton donors of different reactivity. The investigated reactions of reduced forms of *Fnone* include disproportionation with pristine *Fnone* as well as associative interactions and proton transfers, demarcated by acidity constants of intermediates. The possibility of back process, namely hydrogen extraction, was illustrated by chemical activation of loaded carrier molecule.

2. Experimental

2.1. Reagents

Anhydrous dimethylformamide (DMF), tetrabutylammonium tetrafluoroborate (TBABF₄), *Fnone*, *Fmol*, sodium ethoxide (EtONa), methanol, ethanol (EtOH), trifluoroethanol (TFE), deuterium-substituted TFE (TFE-D), hexafluoropropanol-2 (HFP) were purchased from Sigma Aldrich and used as received. Aqua(6,6'-dihydroxy-2,2'-bipyridine)(pentamethylcyclopentadienyl) iridium (III) bis(triflate) (BP-Ir(III) OTf) was purchased from Kanto Chemical Co. and used as received.

2.2. Procedures

2.2.1. Electrochemistry

BioLogic SP200 potentiostat was used for all the electrochemical measurements. Ag/Ag⁺ (silver wire in 0.1 M AgNO₃ in 0.1 M TBABF₄ solution in DMF) and a Pt mesh were used as reference and counter electrodes, respectively. Glassy carbon disk was used as a working electrode. Silver wire in 0.01 M AgNO₃ solution in 0.1 M TBABF₄ in DMF was used as a membrane-separated reference electrode. 85% of ohmic drop correction (determined by a high frequency impedance (50 kHz, 20 mV amplitude)) was performed prior to each voltammetry measurements on film working electrodes.

The simulation of cyclic voltammograms was done by DigiSim version 3.03 electrochemical simulation software (BAS Inc.).

2.2.2. In-situ UV-vis-NIR

The *in-situ* UV-vis spectroelectrochemistry measurements were carried out using 10 mm quartz cuvette with a honeycomb Spectroelectrochemical Cell Kit (Pine Research Instrumentation Inc., USA). The absorption spectra were recorded in the potential window of -0.2 to -2.8 V at 100 mV intervals using Lambda 900 spectrophotometer (PerkinElmer). Operando kinetic spectroelectrochemistry was recorded with an Avantes Avaspec-ULS-2048L fiber optic spectrometer coupled with an Avalight-HAL-S-Mini halogen light source. The kinetic spectra were recorded by reflecting the incident beam from a gold electrode immersed into the electrolyte solution to limit the effects of diffusion on the time response. The absorbance spectra were calculated as $A(t) = -\log[R(t)/R_0]$, where R_0 is the reflected baseline intensity measured at 0.0 V and the reflectance of light $R(t)$ was measured as a function of time after applying either -1.4 or -2.8 V. The kinetic spectra were measured in the range 400–1050 nm with an integration time of 1.25 ms per scan and averaged over 80 scans to achieve a time resolution of 100 ms per spectrum.

2.2.3. In-situ attenuated total reflection-Fourier transform infrared (ATR-FTIR) spectroscopy

ATR-FTIR spectra were collected in a Bruker Vertex 70 spectrometer with a PIKE MIRacle accessory with an open electrochemical cell using a diamond-coated ZnSe crystal and a DLaTGS detector at steady-state regime of electrolysis at potential intervals of 100 mV. Spectra were recorded with a resolution of 4.0 cm^{-1} and by adding 64 scans for each spectrum.

2.2.4. Electronic spin resonance (ESR)

The ESR vs. potential measurements were carried out using Joel JES-FA 200 EPR instrument and AutoLab PGSTAT 20 potentiostat in a tube-type three electrode cell (0.3 mm diameter) with Pt working electrode and Ag and Pt wires as reference and auxiliary electrodes, respectively. Potentials were calibrated with ferrocene standard. All solutions were de-aerated with Ar gas prior to the experiments. The g -factor value was determined with the aid of JEOL internal Mn-standard. Further analysis was done by ESR spectra simulation using WinSim software.

2.2.5. ^1H -nuclear magnetic resonance (NMR) spectroscopy

^1H NMR measurements were performed on dry samples obtained after solvent removal by rotary evaporation at 500 MHz with an Inova Varian Oxford AS500 spectrometer. The analysis was performed in CDCl_3 with chemical shifts referenced against CDCl_3 residual peak at 7.26 ppm or DMF 8.02 ppm [9,10]. Data were processed with MestReNova 12.04–22023 (Mestrelab Research).

2.2.6. Chromatography

The gas analysis was performed by gas chromatography with an Agilent 990 Biogas MicroGC. The high performance liquid chromatography (HPLC) measurements were performed on Waters 515 HPLC Pump equipped with Waters 2424 Evaporative Light Scattering Detector and a SQ Detector 2. High Resolution Mass Spectra and UV-Vis spectra were obtained using a water/acetonitrile mobile phase.

2.2.7. Dehydrogenation of *FnoI*

The dehydrogenation reaction was carried out in a sealed flask with 0.5 M solution (10 mL) of *FnoI* in DMF with addition of the catalyst (BP-Ir(III) OTf, 100 mg). All the connections were tested using soapy water to make sure there is no leakage for released gas. The syringe was employed to collect the gas samples of the

head space. The flask was heated at $80\text{ }^\circ\text{C}$ for an hour followed by cooling to room temperature before measurement.

3. Results and discussion

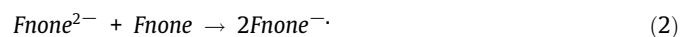
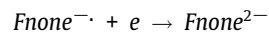
3.1. Redox process of the empty carrier

We start from the investigation of the carrier molecule in the absence of any proton donors in the electrochemical system. Cyclic voltammograms (CV) of *Fnone*, at different media conditions, were examined on glassy carbon electrodes in the dry aprotic solvent dimethylformamide. Two redox peak are observed (Fig. 2a) and are assigned to the consecutive single electron transfers yielding the radical-anion (*Fnone* $^{\cdot-}$, redox process I) and the di-anion *Fnone* $^{2-}$ (redox process II) [11–16] (Scheme 1). Those two processes I and II are diffusion-limited as the current scales with the square root of the scan rate (Fig. S1). The minor cathodic peak (-1.3 V) disappears as the scan rate increases, which is due to the slow reduction of oxygen acting as a contaminant. A similar CV behavior with two consecutive and discrete single electron transfers is typically found for most organic redox molecules in aprotic media, such as for quinones [17] in dimethylformamide. The reversibility and peak height of the redox process I are found to be higher than the redox process II. Indeed, the redox process II exhibits then a larger peak-to-peak potential separation and shows less symmetry in peak currents. The smaller peak heights of the redox process II (Fig. 2a) are archetypical for organic redox molecules and are assigned to the associative behavior of the di-anion [17].

ESR shows the appearance of characteristic spin ($g = 2.00378$) upon the application of negative potentials (-1.4 and -2.8 V) (Supporting Note 1), concomitant to the optical absorbance changes reported below, while no spin is observed at 0 V. This confirms that the red-colored product is indeed the radical-anion of *Fnone* $^{\cdot-}$ generated via a single electron reduction of *Fnone*.

The kinetics of radical-anion formation at these two potentials can be followed in Fig. 2(b) showing the time evolution of the integrated ESR intensity normalized by the recorded total charge measured at the electrode during the entire potential step. It was observed that this potentiostatic total charge at -2.8 V was ca. a factor of two higher than at -1.4 V. According to the cyclic voltammogram (Fig. 2a), only reduction I, *Fnone* + $e^- \rightarrow \text{Fnone}^{\cdot-}$ can take place at -1.4 V, converting an injected electron into an unpaired spin detectable by ESR. When the potential step to -2.8 V is applied to *Fnone* solution, both one-electron reductions I and II take place, which explains twice higher charge. This implies consumption of the radicals created by reduction I via reduction II to a closed-shell di-anion, *Fnone* $^{\cdot-}$ + $e^- \rightarrow \text{Fnone}^{2-}$. However, the rate of *Fnone* $^{\cdot-}$ formation, monitored by both *in-situ* ESR (Fig. 2b), increases to over 2 ($1.9/0.8 = 2.35$) per injected electron for this potential change (-1.4 to -2.8 V), suggesting that reduction II also somehow leads to radicals. In agreement with the ESR, as the applied potential changes from -1.4 to -2.8 V, the rate of *Fnone* $^{\cdot-}$ formation monitored by absorbance at 550 nm (Fig. S3C) increases.

By taking into account that the second electron transfer increases the basicity and reactivity of the spin-invisible di-anion *Fnone* $^{2-}$, the only candidate for this additional exergonic (spontaneous and electrical energy-free) reaction contributing to process II for *Fnone* $^{\cdot-}$ formation is then the di-anion comproportionation with abundant *Fnone* (Inset in Fig. 2a), making it to duplicate effectively process I via a two-stage mechanism:



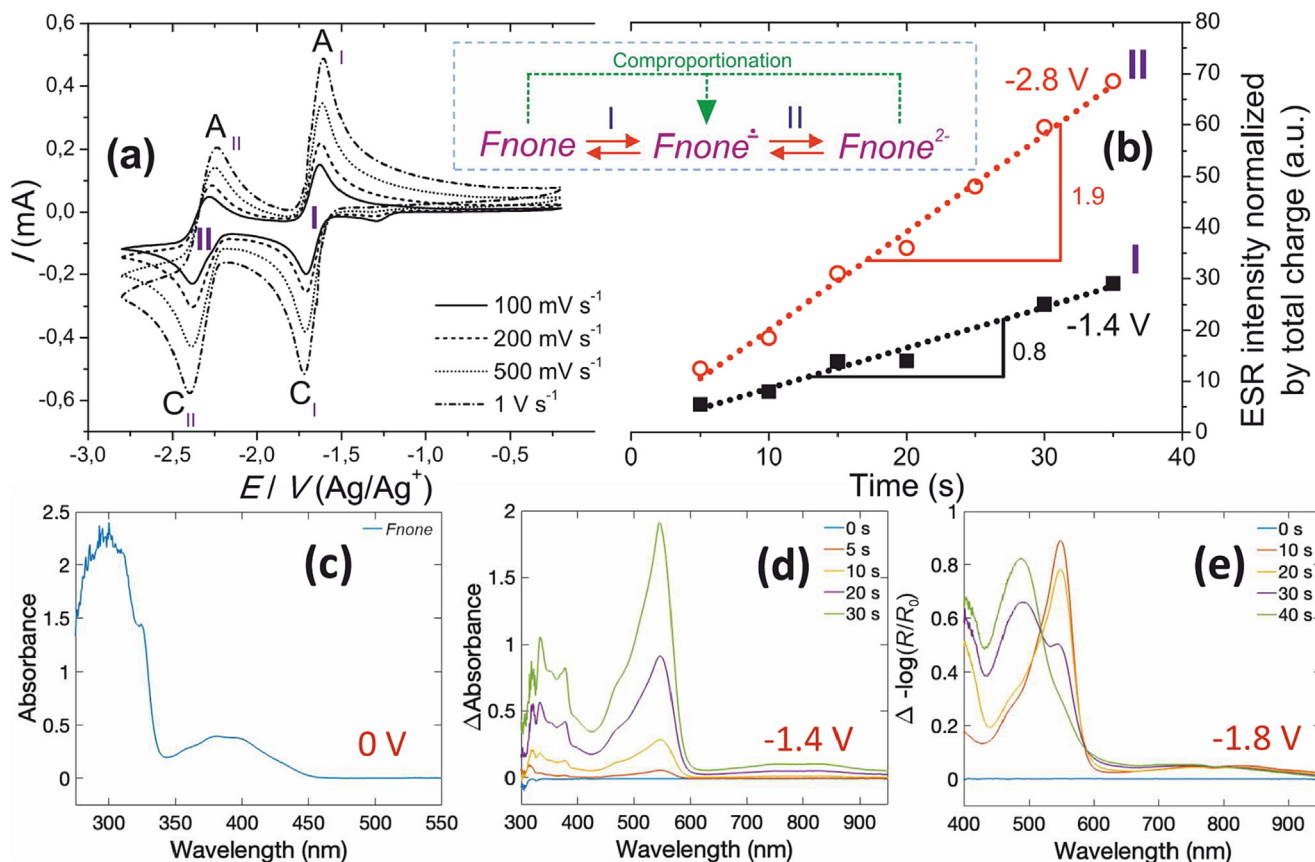


Fig. 2. Redox transformations of carrier molecule. (a) The voltammograms acquired in *Fnone* solution in DMF at different scan rates (0.01 M *Fnone* in 0.1 M TBABF₄, GCE; Inset: the scheme of the comproportionation ($Fnone^{2-} + Fnone \rightarrow 2Fnone^{-}$)); (b) the time dependence of charge-normalized ESR intensity acquired at -1.4 and -2.8 V (black filled and red open symbols, respectively); (c) absorption spectrum of *Fnone* measured in transmission mode (honeycomb electrode); (d) differential absorption spectra of *Fnone* measured in transmission mode (honeycomb electrode) during the application of -1.4 V; (e) differential absorption spectra of *Fnone* measured in reflectance mode (Au mirror electrode) during the application of -1.8 V. Similar measurements for *Fnone* held at -2.8 V are shown in Fig. S13B.

As this chemical reaction consumes the di-anion, it decreases the reversibility of the redox process II, as indicated by the lower oxidation peak current A_{II} (Fig. 2a) compared to the oxidation peak current A_I . By increasing the voltammetry scan rate, the di-anion uptake via reaction (2) lowers, which increases the reversibility (Fig. 2a). We believe that the uptake of the di-anion, via comproportionation with abundant pristine reagent, is a general mechanism behind the low reversibility of the second mono-electronic transfer in these organic molecules in aprotic solvents [18,19].

In-situ UV–Vis–NIR shows two absorption bands of pristine *Fnone* (Fig. 2c), a weaker broad band with a maximum at 380 nm and a more intense band with a maximum at 300 nm and a shoulder at 320 nm. First, we apply a voltage just at the beginning of the first reduction peak, i.e., at -1.4 V, on honeycomb electrode in transmission mode. Multiple positive absorption bands arise (Fig. 2d), assigned here to the absorption of the *Fnone* radical-anion ($Fnone^{-}$). The most intense band has a maximum at 550 nm and a secondary shoulder around 460 nm, with multiple weaker bands visible below 400 nm and a broad and weak absorption band centered around 800 nm. To induce larger absorption changes and to probe the reaction dynamics at the shorter time scale, we switched to reflection mode *in-situ* absorption measurements at a larger surface area gold mirror electrode (Fig. 2e). Although the set-up is limited in the UV region, we are able to detect new absorption signals when the applied voltage is more negative at -1.8 V. Initially, after applying this potential, the same positive absorption feature as at -1.4 V (Fig. 2d) grows with a max-

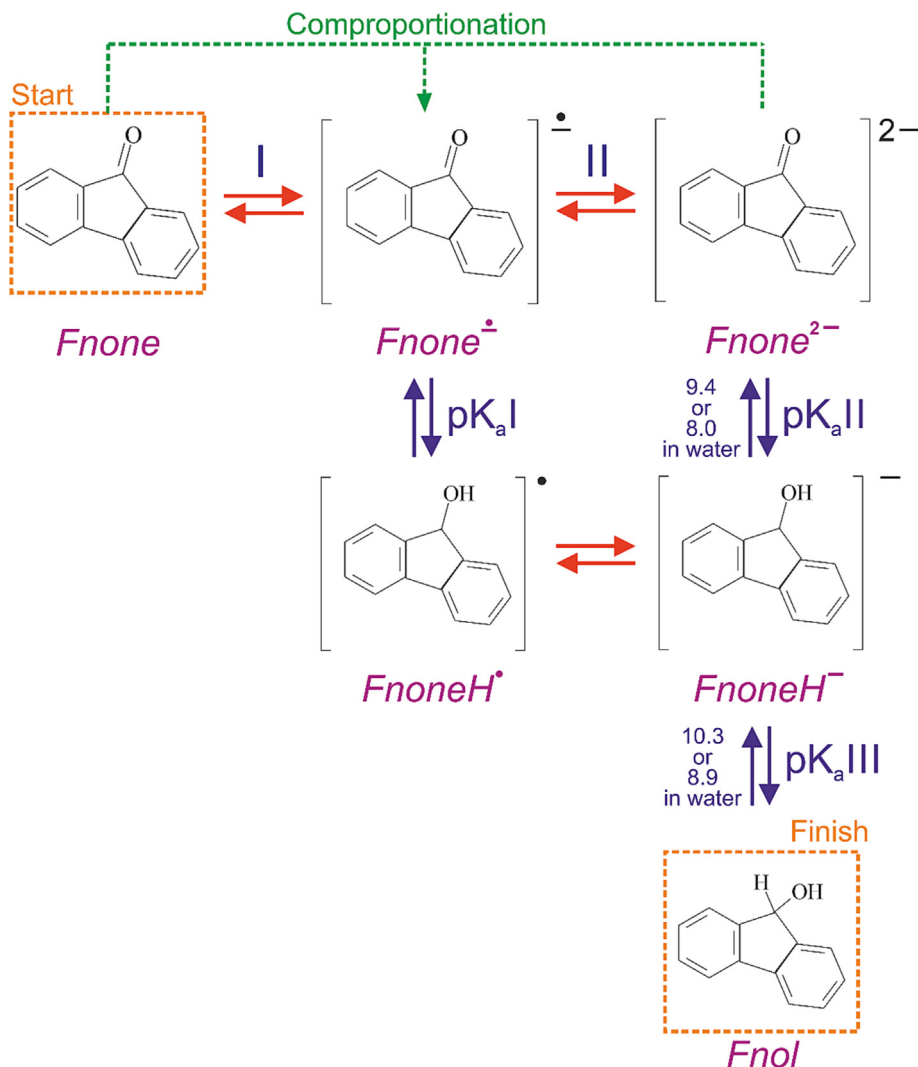
imum at 550 nm, indicative of the formation of $Fnone^{-}$. However, the longer elapsed times of electrolysis lead to spectral evolution with a few isosbestic points maintained. The $Fnone^{-}$ absorption progressively decreases while a new absorption feature with a maximum at 490 nm is formed (Fig. 2e). The appearance of isosbestic points manifests 1:1 stoichiometry of $Fnone^{-}$ transformation to the new species, which is not a pristine *Fnone*. We assign this new absorption to originate from *Fnone* di-anion ($Fnone^{2-}$). We explain the dynamics of this spectra evolution by sequential electrochemical reduction of $Fnone^{-}$ after the *Fnone* exhaustion in the vicinity of the electrode. The similar processes at much faster rates were observed when the applied potential is much more negative (-2.8 V, Fig. S3C).

In-situ ATR-FTIR spectroelectrochemistry support the conversion of the carbonyl moiety due to the formation of di-anion, visible as the reduction of carbonyl peak intensity (Fig. S4C) with increase of electrolysis potential, in comparison with the spectrum acquired in *Fnone* solution without electrolysis.

The electrochemical reduction of carrier molecule in aprotic media generates the species of various basicity. Reactivity of these electrogenerated species in proton transfer reaction as a key step in EHS can be probed by the use proton donors of different strengths.

3.2. Electrochemical hydrogen storage in the LOHC

Now that we understand the redox properties of *Fnone* in solution as LOHC, we begin investigating the mechanism of EHS. Sim-



Scheme 1. The scheme of *Fnone* electrochemical hydrogenation. Red and blue arrows represent electron and proton transfers, respectively; green dashed arrow – comproportionation reaction; the values pK_a for the *FnoneH*-associated acid–base equilibria (pK_{aII} and pK_{aIII}) are derived from computed data from [23] (Table 1S).

ilarly to quinones [20–22], *Fnone* hydrogenation due to the reaction (1) implies transfers of two electrons, which are coupled to transfers of two protons (Scheme 1). Interestingly, the values of the first and second acid dissociation constants of *FnoneH* are inverted (Table 1S) [23] due to the involvement of ketone group in the conjugation system of *Fnone*. This is manifested by the higher basicity of the pristine alcohol *FnoneH* with respect to its anionic form *FnoneH*[−].

We focus on the investigation of the role of hydrogen-bonding agents (HBAs) as proton source for the proton transfer reaction with electrogenerated reduced species (*Fnone*^{•−} and *Fnone*^{2−}) of the carrier molecule (*Fnone*) in an aprotic solvent. The interaction between the HBA and the reduced form of LOHC is a key factor to control the ESH.

The basicity of both the *Fnone*^{•−} and *Fnone*^{2−} favors the interactions with Lewis [12–16] and Brønsted acids [24,25]. The non-specific (associative) interactions are ion-pairing with electrolyte ions [17,26] and re-solvation by a polar solvent [17,27,28]. In contrast, the specific interactions are the chemical reactions of the radical-anion and the di-anion that produce the chemical transformations, such as the hydrogenation, manifesting the making or breaking chemical bonds. We utilized three dry HBAs (weak Brønsted acids) of different acidity (Table 1) [29–32] as proton

Table 1
 pK_a values of HBAs.

HBA	pK_a (in water)*	pK_a (in solvent)
Ethanol (EtOH)	15.9	29.8 (DMSO) [32]
Water	15.7	32 [31]
Trifluoroethanol (TFE)	12.4	23.6 [31]
Hexafluoropropanol-2 (HFP)	9.3	18.9 (DMF) [30]

* [17,29].

sources for a systematic investigation of the EHS of the LOHC (Scheme 1): ethanol (EtOH), trifluoroethanol (TFE), hexafluoropropanol-2 (HFP).

3.3. Non-specific interactions

The changes of the potentials of redox peak couples on CV manifest the interactions of corresponding species with the solution environment. The addition of an equimolar concentration of the weakest proton donor (EtOH) leads to no change in the positions of the redox peak currents of processes I and II (Fig. 3a). However, further incremental increase of EtOH concentration leads to a sys-

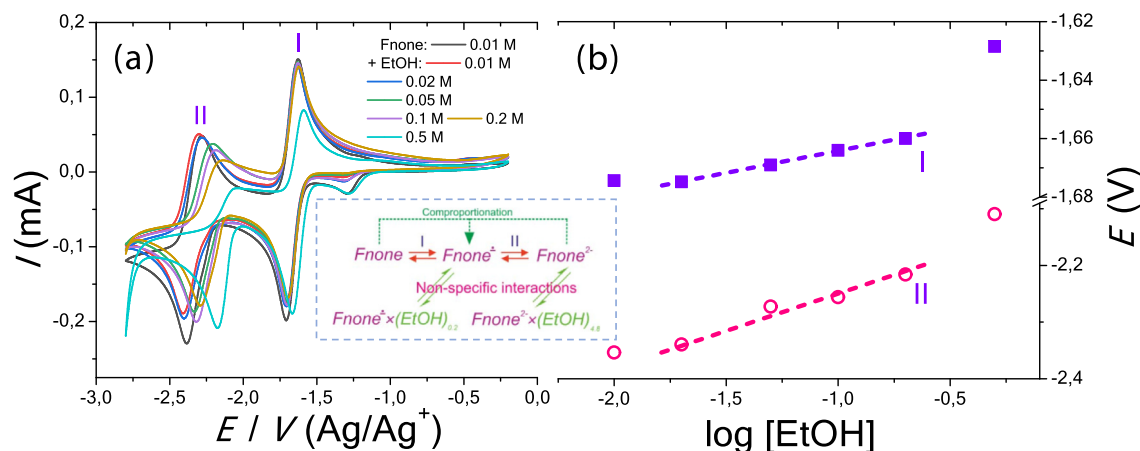


Fig. 3. The non-specific interactions of reduced species of carrier molecule. (a) The voltammograms in presence of different concentrations of EtOH (scan rate 100 mV s⁻¹, GCE); (b) the dependence of the midpoint potentials of the redox processes I and II on the EtOH content; Insert: the scheme of the non-specific interactions.

tematic positive displacement for both peaks (Fig. 3b). The reversibility for both redox processes even up to a 10 times excess in EtOH illustrates *non-specific* interactions (e.g., hydrogen-bonding) of $Fnone^{\cdot-}$ and $Fnone^{2-}$ with this weak HBA [17]. The absence of any impact on the $Fnone^{\cdot-}$ ESR signal (Fig. S5A) upon adding the excess of a weak HBA (methanol in 100 times excess) indicates the presence of the intact radical-anion; thus revealing the associative character of the interactions with EtOH instead of direct proton transfer from EtOH to the reduced species of Fnone. This leads to the formation of two complexes, i.e., $Fnone^{\cdot-}(EtOH)_{0.2}$ and $Fnone^{2-}(EtOH)_{4.8}$ (Supporting Note 2, Inset in Fig. 3). Other known non-specific (associative) interactions are e.g., ion-pairing with electrolyte ions [17,26] and re-solvation by a polar solvent [17,27,28].

Because the goal is to promote the hydrogenation of the reduced fluorenone, stronger acids (TFE and HFP) need to be added to the Fnone solution. We expect to find specific interactions leading to the irreversible (electro)-chemical reactions of the radical-anion and the di-anion with the proton that yield hydrogenation.

3.4. Specific interactions: enabling proton transfer reaction on di-anion

We then investigated the interaction of the carrier molecule reduced species with TFE (Fig. 4), which is a mild HBA, though stronger than EtOH due to high electronegativity of the fluorine atoms. Reaching close-to-equimolar concentrations leads to peak II splitting (Fig. 4a), while peak I remains unaffected. The observed peak II splitting might be due to co-existence of two processes involving protonated and non-protonated forms because of the significant deceleration of the proton transfer rates at the time scale of CV (Supporting Note 3) [33,34]. We attribute this to low buffer capacity in aprotic media due to the absence of buffer assuring the fast achievement of acid–base equilibria. At the same time, this rules out non-specific interactions in equilibria and underscores the appearance of the protonated form of di-anion $Fnone^{2-}$ in the presence of TFE, in contrast to the weak proton donor (EtOH, Fig. 3a).

In coherence with experimental observations, the simulated CV (Fig. S8) showed the splitting of both the oxidation and reduction peaks of the redox process II with the appearance of the irreversible conversion of both $Fnone^{\cdot-}$ and $Fnone^{2-}$.

Increasing the concentration of TFE allows to attain the protonation of less basic form $Fnone^{\cdot-}$ (lower pK_a I, Scheme 1) in addition to more basic di-anion $Fnone^{2-}$ (lower pK_a II, Scheme 1). Higher

Brønsted basicity of di-anion $Fnone^{2-}$ in comparison with $Fnone^{\cdot-}$ explains the higher impact of the reaction with proton donor at close-to-equimolar concentrations. According to operando ESR spectroelectrochemistry, the rates of $Fnone^{\cdot-}$ generation via comproportionation of di-anion $Fnone^{2-}$ (redox process II at -2.8 V, Fig. 4b) and via direct redox process I (at -1.4 V Fig. 4b) are almost the same in the presence of equimolar TFE concentrations. Recall that in the absence of proton donors, as well as in even 100 times excess of the weak donor (MeOH), comproportionation resulted in a significantly higher intensity of $Fnone^{\cdot-}$ (at -2.8 V, Fig. S5A). We conclude that the neutralization of $Fnone^{2-}$ by TFE disables its comproportionation, which is manifested by a decrease of the reaction rate of $Fnone^{\cdot-}$ formation at -2.8 V, while process I, at -1.4 V, remains almost intact (Fig. 4b).

3.5. Specific interactions: enabling proton transfer reaction on radical-anion

Fnone reduced at -1.4 V does not display any change in its absorption spectra within 80 s (Fig. 4c) in a honeycomb electrode architecture because of the slow diffusion from electrode surface to the optical detection volume. In contrast, in presence of an excess of TFE (Fnone: TFE with 1:50 molar ratio), the spectrum displays a clear disappearance of pristine Fnone evidenced by gradual decrease of its absorption bands (380 and 320 nm). Note that the absorption band centered at 300 nm is almost unaffected and relates to the benzene rings of Fnone that remains intact. Hence it is mostly the ring with the ketone which is affected by the reduction in presence of TFE. This suggests that TFE, its acidic proton in this context, reacts with the radical-anion $Fnone^{\cdot-}$ formed upon electrochemical reduction of Fnone.

In contrast to the negative dynamics of Fnone-specific bands in differential absorption (380 and 320 nm, Fig. 4d), the new absorption in the region 450–550 nm appears, which corresponds to the absorption region of $Fnone^{\cdot-}$, but is different in the distribution of intensities. We suppose therefore that in the absence of TFE, the reduction of Fnone at -1.4 V is dominated by the formation of radical anion $Fnone + e^- \rightarrow Fnone^{\cdot-}$, but in the presence of TFE in excess another product is formed, attributed to the subsequent reaction with the proton of TFE yielding the neutral semi-fluorenone: $Fnone^{\cdot-} + H^+ \rightarrow FnoneH^{\cdot}$.

The differential absorption, which follows the potential step from -1.4 V to open circuit (60 s, Fig. 4e), visualizes the difference in kinetic behavior of various bands. The positive differential absorption at 460, 520 and 800 nm quickly decreases, while the

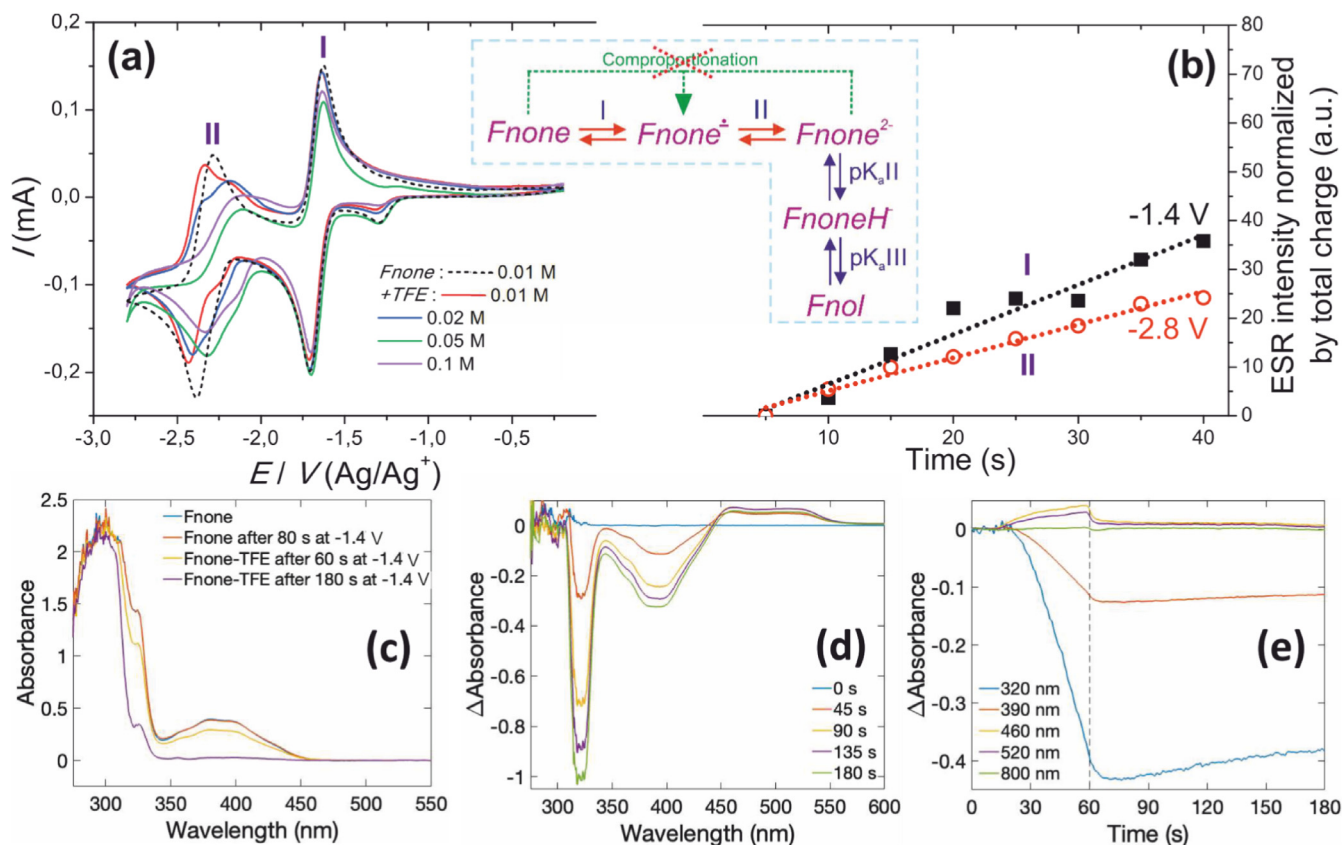


Fig. 4. The proton transfer reaction on Fnone^{2-} . (a) The cyclic voltammograms recorded in absence (dashed black curve) and in presence of small excess TFE (scan rate 100 mV s^{-1} ; GCE, 0.1 M TBABF_4 , 0.01 M Fnone in DMF; Inset: the scheme of specific proton transfer on Fnone^{2-}); (b) the time dependence of charge-normalized ESR intensity acquired during the electrolysis at -1.4 and -2.8 V (black filled and red open symbols, respectively) in $1:10 \text{ Fnone:TFE}$; (c) steady-state absorption spectra 0.01 M Fnone without and with 0.5 M TFE (0.1 M TBABF_4 in DMF) before and after the application of -1.4 V measured in transmission mode (honeycomb electrode); (d) differential absorption spectra of Fnone (0.01 M) in the presence of TFE (0.1 M) measured in transmission mode (honeycomb electrode) during the application of -1.4 V (0.1 M TBABF_4 in DMF); (e) the dynamics of differential absorption spectra at select wavelengths during the application of -1.4 V for 60 s followed by the change of potential to open circuit.

differential absorption at 320 and 390 nm undergoes a delay after the potential is turned off. Therefore, these groups of bands refer to the species of different reactivity. The optical signature of neutral semi-fluorenone FnoneH^\cdot reveals its higher reactivity in comparison with Fnone^\cdot .

The tubular geometry of the honeycomb electrode is featured with two time resolved regimes of diffusion, namely within the cavity and from the outer solution (Supporting Note 4). The switching between the regimes is manifested by the change of the slope of absorbance time dependence, while the time of the

change is a characteristic time of exhaustion of the cavity. This allowed us to estimate the faradaic efficiency of irreversible electrochemical conversion of Fnone as 40.3% .

The use of TFE with deuterium-substituted alcohol atom (TFE-D) showed the decrease of the rate of Fnone^\cdot formation (at -2.8 V , Supporting Note 5). This manifests the out-of-equilibrium behavior of the proton transfer reaction at short time scale in aprotic media of low buffer capacity.

From EtOH to TFE followed by both electron transfer processes I and II become increasingly irreversible in the electrochemical

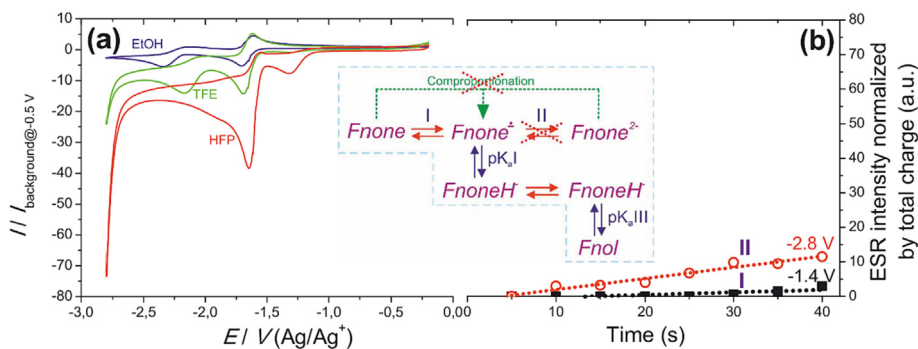


Fig. 5. The proton transfer reaction on Fnone^\cdot . (a) Background-normalized cyclic voltammograms recorded in $1:50$ excess of HBAs (EtOH, TFE and HFP as blue, green and red curves, respectively; scan rate 1 V s^{-1} ; Inset: the scheme of specific proton transfer on Fnone^\cdot); (b) the time dependence of charge-normalized ESR intensity acquired at -1.4 and -2.8 V (black filled and red open symbols, respectively) in $1:50$ of Fnone:TFE .

reduction. While the redox process I remains unaffected, the redox process II shifts to more positive potentials (Fig. 5a). This makes the redox process II a PCET. Now we use a still stronger proton donor, HFP. Both redox processes I and II merge into a unified reduction peak because the redox process II shifts more positively and overlaps with redox process I. The current intensity of this irreversible peak increases considerably with the acidity of HBA. The operando ESR in the presence of excess of TFE (1:50) showed drastic decrease of the radical species production at both -1.4 and -2.8 V. This implies the bypass of $\text{Fnone}^{\cdot-}$ accumulation. Evidently, more basic di-anion Fnone^{2-} is bypassed also. This has also been confirmed by a variety of operando spectroelectrochemistry techniques in both steady-state and short-time regimes of electrolysis (Supporting Note 6). Launching $\text{Fnone}^{\cdot-}$ neutralization with just 5 times increase of the mild HBA concentration (Figs. 4b and 5b) implies close values of pK_aI and pK_aII .

Traditionally, irreversibility of cyclic voltammograms is explained by the irreversible chemical step between two separate transfers of electrons (electron-chemical-electron mechanism, ECE), which implies the change of the reaction pathway. The first electron transfer process yields $\text{Fnone}^{\cdot-}$, which is followed by the irreversible and relatively slower chemical reaction (protonation) that generates neutral semi-fluorenone FnoneH^{\cdot} (Scheme 1). The second electron transfer onto FnoneH^{\cdot} is thermodynamically more favorable than the first electron transfer (so-called potential inversion [35]) leading to the merged two-electron peak. The resulting reaction pathway is then to a larger extent governed by the ' $\text{Fnone}^{\cdot-}$ -to- FnoneH^{\cdot} -to- FnoneH^{\cdot} ' track (Inset in Fig. 5 and Scheme 1) before the ' $\text{Fnone}^{\cdot-}$ -to- Fnone^{2-} -to- FnoneH^{\cdot} ' track (Inset Fig. 4 and Scheme 1) as the mild and strong HBAs concentrations increases.

The successful electrochemical hydrogenation storage in Fnone is illustrated by the detection of Fnl by HNMR (Fig. S14), which displays a specific peak for the C–H of the 5 ring core at 5.7 ppm, as well as an ensemble of peaks at 7.3 ppm. Our estimate is that the efficiency of the reaction $\text{Fnone} + 2e^- + 2\text{H}^+ \rightarrow \text{Fnl}$ is about 2.5%.

3.6. Chemical dehydrogenation of the loaded carrier

3.6.1. Chemical oxidation

The possibility of the back process, namely, Fnl alcohol oxidation to the pristine carrier Fnone , was qualitatively explored by incorporating a base, namely sodium ethoxide ($\text{pK}_a^{\text{H}_2\text{O}}$ 16; $\text{pK}_a^{\text{DMSO}}$ 29.8 [32]), into the Fnl solution in DMF. The appearance of the characteristic ESR signal (Fig. S15) as well as the red color of the solution upon the addition of the base manifests the formation of $\text{Fnone}^{\cdot-}$ as a result of single electron oxidation of de-protonated alcohol (FnoneH^{\cdot}). Here, dissolved oxygen and other contaminants serve as available electron acceptors. Further exposure of the red-colored $\text{Fnone}^{\cdot-}$ solution to ambient air results in a gradual transformation of its color from red to yellow, which testifies the subsequent conversion of $\text{Fnone}^{\cdot-}$ to pristine Fnone . But when a weaker base, namely piperidine ($\text{pK}_a^{\text{DMSO}}$ 10.90 [36]) is added, there is no visible color change. Therefore, both pK_aIII and pK_aI are accessible by stronger bases (Scheme 1). Importantly, the faster kinetics of de-protonated alcohol oxidation, in comparison with the subsequent conversion of $\text{Fnone}^{\cdot-}$ to pristine Fnone by oxygen, suggests a higher reactivity of FnoneH^{\cdot} in comparison with radical-anion oxidation. These experimental observations imply the existence of the back process in a circular Fnone -based EHS (Scheme 1).

3.6.2. Hydrogen release

Finally, we demonstrate the release of hydrogen gas by catalytic dehydrogenation of Fnl into Fnone . It has been demonstrated that transition metal compounds have catalytic activity for dehydrogenative oxidation of alcohols, in an oxidant-free environment [7,37–42]. We confirmed the release of hydrogen gas upon heating

of commercial Fnl in DMF in the presence of catalyst (BP-Ir(III) Otf) quantified by GC and ^1H NMR (Fig. S16). The estimated conversion efficiency about 1.25%, which is close to reported values [7,38], confirming the possibility of catalytic extraction of hydrogen in mild experimental conditions, while the optimization of this process is beyond the scope of this report.

The main advantage of EHS over the chemical hydrogenation of LOHC is that the catalyst-free process proceeds at room temperature and ambient pressure, which is favourable from perspectives of both energy efficiency and carrier molecule stability. The realistic strategy for the large scale EHS is the membrane electrolysis (Fig. 1c) of the carrier at high concentrations [43]. Protons for this conversion would then be supplied through a proton-exchange membrane separating EHS on LOHC from an appropriate proton-coupled auxiliary reaction of oxidation in the other compartment, e.g., hydrogen oxidation reaction (HOR) or oxygen evolution reaction (OER) thus reconstructing the PCET. Note that one carrier molecule may include more than one moiety undergoing PCET leading to higher density EHS on LOHC [44].

As it was shown here, the electrochemical transformations of EHS involve reactive organic radicals prone to side reactions resulting in the losses of carrier molecules. The control of the process conditions, such as electrolysis current densities, mass transport and purity, is needed to minimize these losses. Specifically, electrolysis on PEM at high current densities would ensure abundant proton transfers from strong HBA at high concentrations to the activated carrier assuring its complete electrochemical hydrogenation. In addition, the high purity of the EHS electrolyzer would disable the loss of the loaded carrier by chemical oxidation.

4. Conclusions

To conclude, we presented the concept of EHS on fluorenone as a model for LOHC simplifying the technology of hydrogen storage. The loading of organic carrier molecules, such as quinones, by hydrogen atoms via C–H bond formation can be exemplified by proton-coupled electron transfers at room temperature. The use of aprotic media allowed us to control the proton transfer reactions from proton donors of different strength to activated forms of carrier molecule of different acceptor reactivity. Using the variety of *in-situ* spectroelectrochemical techniques, we testified the comproportionation between pristine molecule and reactive product of two sequential electron transfers, namely di-anion. The consecutive alteration of the mechanism due to launching of proton transfer reactions confirmed our concept of the proton transfer reaction on a product of single electron transfer, namely radical-anion, as an irreversible chemical step preceding the second electron transfer.

The possibilities for the back process, namely hydrogen release, obtained a preliminary demonstration by chemical activation of the commercial loaded carrier molecule. We believe that other LOHC with higher densities of hydrogen loading would be identified opening a new pathway for hydrogen storage technology.

Declaration of competing interest

The authors declare that they have no known competing financial interests or personal relationships that could have appeared to influence the work reported in this paper.

Acknowledgements

This work was financially supported by the Swedish Research Council (grant 2016-05990), the Knut and Alice Wallenberg Foundation (H2O2 and Cellfion) and the Swedish Government Strategic

Research Area in Materials Science on Advanced Functional Materials at Linköping University (Faculty Grant SFO-Mat-LiU No. 2009-00971).

Appendix A. Supplementary data

Supplementary data to this article can be found online at <https://doi.org/10.1016/j.jechem.2022.06.015>.

References

- [1] G. Nicoletti, N. Arcuri, G. Nicoletti, R. Bruno, *Energy Convers. Manage.* 89 (2015) 205–213.
- [2] B. Sakintuna, F. Lamari-Darkrim, M. Hirscher, *Int. J. Hydrogen Energy* 32 (2007) 1121–1140.
- [3] J. Puszkiel, S. Garroni, C. Milanese, F. Gennari, T. Klassen, M. Dornheim, C. Pistidda, *Inorganics* 5 (2017) 74.
- [4] M. Niermann, S. Timmerberg, S. Drünert, M. Kaltschmitt, *Renew. Sustain. Energy Rev.* 135 (2021) 110171.
- [5] X.Y. Zhao, L.Q. Ma, *Int. J. Hydrogen Energy* 34 (2009) 4788–4796.
- [6] Y.F. Liu, H.G. Pan, M.X. Gao, Q.D. Wang, *J. Mater. Chem.* 21 (2011) 4743–4755.
- [7] R. Kato, K. Yoshimasa, T. Egashira, T. Oya, K. Oyaizu, H. Nishide, *Nat. Commun.* 7 (2016) 13032.
- [8] C. Costentin, M. Robert, J.M. Saveant, *Acc. Chem. Res.* 43 (2010) 1019–1029.
- [9] H.E. Gottlieb, V. Kotlyar, A. Nudelman, *J. Org. Chem.* 62 (1997) 7512–7515.
- [10] F. Malz, H. Jancke, *J. Pharm. Biomed.* 38 (2005) 813–823.
- [11] G.T. Cheek, *ECS Trans.* 58 (2014) 45–51.
- [12] G.T. Cheek, *ECS Trans.* 45 (2013) 23–27.
- [13] G.T. Cheek, *ECS Trans.* 35 (2011) 17–21.
- [14] G.T. Cheek, *ECS Trans.* 25 (2010) 117–121.
- [15] G.T. Cheek, *ECS Trans.* 33 (2010) 509–514.
- [16] D. Canby, E. Sanders, G.T. Cheek, *J. Electrochem. Soc.* 160 (2013) G3159–G3164.
- [17] N. Gupta, H. Linschitz, *JACS* 119 (1997) 6384–6391.
- [18] M.W. Lehmann, D.H. Evans, *J. Electroanal. Chem.* 500 (2001) 12–20.
- [19] A. Rene, D.H. Evans, *J. Phys. Chem. C* 116 (2012) 14454–14460.
- [20] J. Jacq, *J. Electroanal. Chem. Interfacial Electrochem.* 29 (1971) 149–180.
- [21] E. Laviron, *J. Electroanal. Chem.* 146 (1983) 15–36.
- [22] Q.Q. Lin, Q. Li, C. Batchelor-McAuley, R.G. Compton, *J. Phys. Chem. C* 119 (2015) 1489–1495.
- [23] A.S. Mendkovich, M.A. Syroeshkin, D.V. Nasybullina, M.N. Mikhailov, V.P. Gulyai, M.N. Elinson, A.I. Rusakov, *Electrochim. Acta* 191 (2016) 962–973.
- [24] J. Bessard, G. Cauquis, D. Serve, *Electrochim. Acta* 25 (1980) 1187–1197.
- [25] M. Bauscher, W. Mantele, *J. Phys. Chem.* 96 (1992) 11101–11108.
- [26] C. Russel, W. Jaenicke, *J. Electroanal. Chem.* 199 (1986) 139–151.
- [27] J.H. Wilford, M.D. Archer, *J. Electroanal. Chem.* 190 (1985) 271–277.
- [28] J.S. Jaworski, E. Lesniewska, M.K. Kalinowski, *J. Electroanal. Chem.* 105 (1979) 329–334.
- [29] M.H. Abraham, P.P. Duce, D.V. Prior, D.G. Barratt, J.J. Morris, P.J. Taylor, *J. Chem. Soc., Perkin Trans. 2* (1989) 1355–1375.
- [30] K.S. Alleman, D.G. Peters, *J. Electroanal. Chem.* 460 (1999) 207–213.
- [31] F.G. Bordwell, *Acc. Chem. Res.* 21 (1988) 456–463.
- [32] W.N. Olmstead, Z. Margolin, F.G. Bordwell, *J. Org. Chem.* 45 (1980) 3295–3299.
- [33] M. Quan, D. Sanchez, M.F. Wasylkiw, D.K. Smith, *JACS* 129 (2007) 12847–12856.
- [34] J. Wang, L. Wang, Y. Wang, W. Yang, L. Jiang, E. Wang, *J. Electroanal. Chem.* 601 (2007) 107–111.
- [35] C. Batchelor-McAuley, R.G. Compton, *J. Electroanal. Chem.* 669 (2012) 73–81.
- [36] M.R. Crompton, I.A. Robotham, *J. Chem. Res.-S* 1 (1997) 22–23.
- [37] K. Fujita, R. Tamura, Y. Tanaka, M. Yoshida, M. Onoda, R. Yamaguchi, *ACS Catal.* 7 (2017) 7226–7230.
- [38] R. Kawahara, K. Fujita, R. Yamaguchi, *JACS* 134 (2012) 3643–3646.
- [39] Y. Kim, S. Ahn, J.Y. Hwang, D.H. Ko, K.Y. Kwon, *Catalysts* 7 (2017) 7.
- [40] J.K. Mobley, M. Crocker, *RSC Adv.* 5 (2015) 65780–65797.
- [41] P. Wu, L. Song, Y. Wang, X. Liu, Z. He, P. Bai, Z. Yan, *Appl. Surf. Sci.* 537 (2021) 148059.
- [42] E. Yazdani, A. Heydari, *J. Organomet. Chem.* 924 (2020) 121453.
- [43] N. Itoh, W.C. Xu, S. Hara, K. Sakaki, *Catal. Today* 56 (2000) 307–314.
- [44] G.T. Cheek, *J. Electrochem. Soc.* 164 (2017) H5160–H5164.